A Goniometric Microscope to Quantify Feather Structure, Wettability, and Resistance to Liquid Penetration

Siddarth Srinivasan,[†ψ] Shreerang S. Chhatre,[†ψ] Jesus O. Guardado,[‡] Kenneth (Kyoo-Chul) Park,[§] Andrew R. Parker,[£] Michael F. Rubner, [‡] Gareth H. McKinley,[§*] and Robert E. Cohen[†*]

† - Department of Chemical Engineering,

‡ - Department of Materials Science and Engineering,

§ - Department of Mechanical Engineering, Massachusetts Institute of Technology, Cambridge MA 02139

£ - Department of Life Sciences, Natural History Museum, Cromwell Road, London, SW7 5BD, UK

ψ – Indicates equal contribution

Corresponding authors: *

Prof. Gareth H. McKinley, Building 3-250, 77 Massachusetts Avenue, Cambridge, MA 02139, phone: (617) 258-0754, email – gareth@mit.edu

Prof. Robert E. Cohen, Building 66-554, 77 Massachusetts Avenue, Cambridge, MA 02139, phone: (617) 253-3777, email – recohen@mit.edu

Abstract

Birds in the cormorant (*Phalacrocoracidae*) family dive tens of meters into water to prey on fish while entraining a thin layer of air (a plastron film) within the microstructures of their feathers. In addition, many species within the family spread their wings for long periods of time upon emerging from water. To investigate whether wetting and wing spreading are related to feather structure, extensive microscopy and photographic studies have been employed to extract structural parameters for barbs and barbules. In this work, we propose an alternative to microscopy and describe a systematic methodology to characterize the quasi-hierarchical topography of bird feathers that is based on contact angle measurements using a set of polar and non-polar probing liquids. Contact angle measurements on dip-coated feathers of six aquatic bird species (including three from the *Phalacrocoracidae* family) are used to extract two distinguishing structural parameters, a dimensionless spacing ratio of the barbule (D^*) and a characteristic length scale corresponding to the spacing of defect sites. The dimensionless spacing parameter can be used in conjunction with a model for the surface topography to enable us to predict *a priori* the apparent water contact angles as well as the water breakthrough pressure for the disruption of the plastron on the feather barbules. The predicted values of breakthrough depths in water (1-4 m) are towards the lower end of the spectrum of the typical depth of diving for the aquatic bird species examined here, and therefore a representative feather is expected to be fully wetted in a typical deep dive. However, thermodynamic surface energy analysis based on a simple 1-D cylindrical model of the feathers using parameters extracted from the goniometric analysis reveals that for water droplets on feathers of all six species under consideration, the non-wetting 'Cassie-Baxter' composite state represents the global energy minimum of the system. By contrast, for other wetting liquids, such as alkanes and common oils, the global energy minimum corresponds to a fully-wetted or Wenzel state. For diving birds, individual feathers will therefore spontaneously dewet once the bird emerges out of water, and the "wing spreading" posture might assist in overcoming kinetic barriers associated with pinning of liquid droplets that retard the rate of drying of the wet plumage of diving birds.

1. Introduction

The water-repellent nature of various bird feathers is typically attributed to a combination of a natural hydrophobic coating (preen oil) coupled with the microstructural topography of the feathers (1). A droplet that is deposited on a water-repellent feather resides in a solid-liquid-air non-wetting composite state, where tiny air pockets are trapped within the barbules of the feathers. These air pockets appear shiny when immersed under a liquid and are referred to as a plastron. While the term plastron was initially formulated by Brocher (2) to describe a general thin film of gas, it has primarily been studied in the context of aquatic insects where the utility of the plastron-like air layer in hiding from predators, for respiration, for mating, or for providing a safe habitat for their young has been extensively investigated (3-9).

In aquatic birds, the existence of this plastron air layer inhibits the complete wetting of the feather and is thought to be critical in maintaining its water repellency. A plastron layer around the plumage also enhances insulation, ensures adequate thermoregulation, and can provide additional buoyancy to aquatic birds (10, 11). Birds in the cormorant family routinely dive in water up to many tens of meters for food and are known to subsequently dry their wings by spreading them in sunlight for extended periods of time. Noting this behavior, researchers have attempted to correlate the diving and wing spreading phenomena to the structure of bird feathers, with notable efforts for the cormorant and darter, but there is lack of a clear consensus (12-15). In their seminal paper on the wettability of porous substrates, Cassie and Baxter (16) recognize the applicability of their idealized cylindrical model in describing the wetting on the barbules of bird feathers. Subsequently, Rijke correlated the feather structure and wing spreading phenomenon by documenting the wing-spreading behaviors of cormorants and studying feather barbs and barbules, which he characterized by applying the Cassie-Baxter model to feather texture (12).

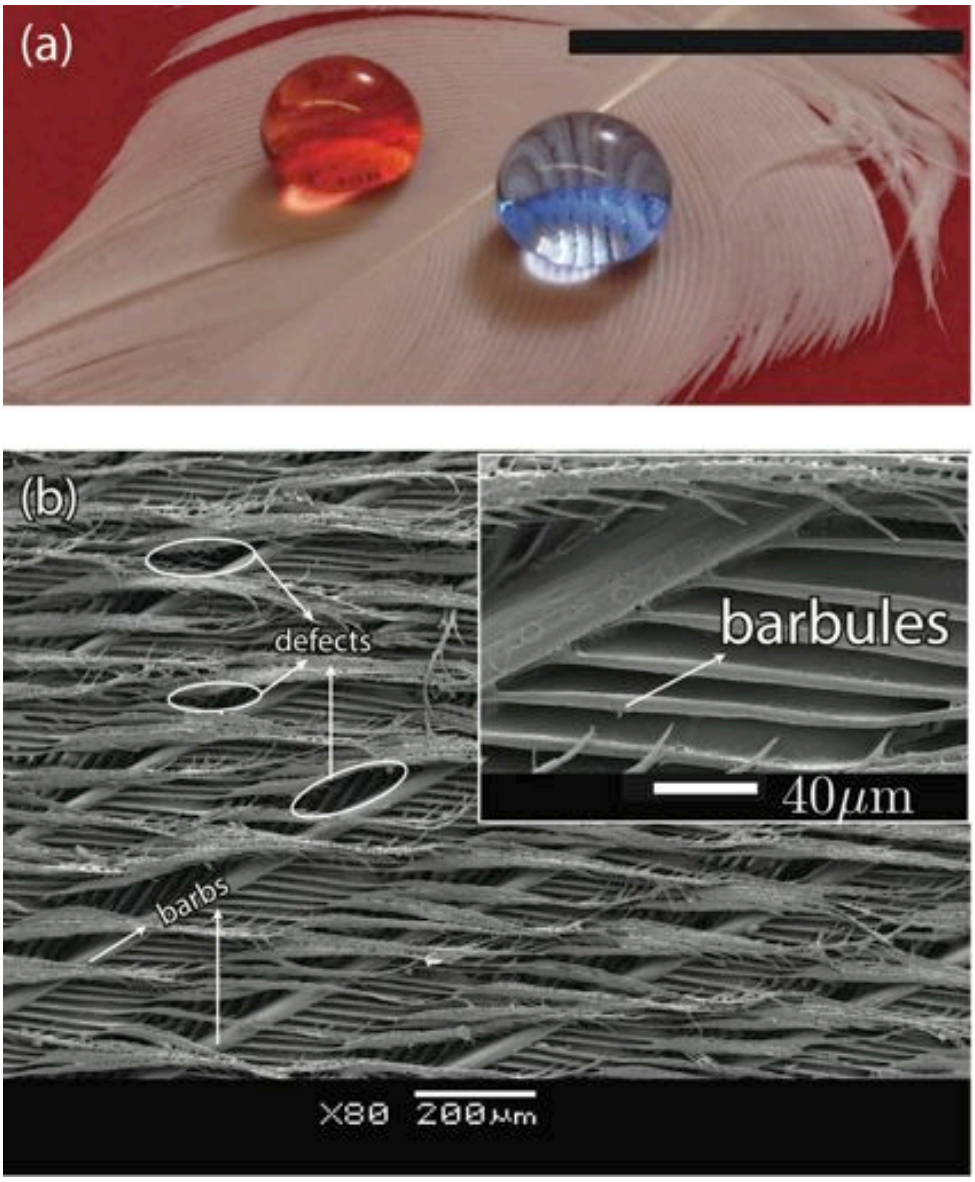

Figure 1. (a) A wing feather of a Common Shelduck after dip-coating in 50-50 fluorodecyl POSS/Tecnoflon solution is not wetted by water (γ_{lv} = 72.1 mN/m, colored blue), or rapeseed oil (γ_{lv} = 35.5 mN/m, colored red). The scale bar in the figure corresponds to 1 cm. (b) SEM image of the wing feather of a Great Cormorant indicating the complex 'quasi-hierarchical' structure of the feather (17) characterized by multiple length scales corresponding to the barbs, barbules (inset) and defect sites.

Bird feathers have cylindrically-shaped barbs and barbules that emerge from the main shaft (*rachis*) of the feather. Rijke employed optical microscopy and photography to measure barb spacing, *2D*, and diameter, *2R*, from which he calculated a spacing ratio $D^* = (R+D)/R$ for various bird species (12). In previous literature, researchers have argued both in favor of, and against, a correlation between the spacing ratio D^* for the feathers and diving, swimming, and wing-spreading behavior (18-21). Recently, Bormashenko (17) obtained an estimate of the water breakthrough pressure on typical feathers as ~ 10 kPa (corresponding to a diving depth of ~ 1 m). Past studies have also relied on photographic and microscopic techniques in attempts to characterize feather structure and wettability (12, 14, 18, 19, 22, 23).

In this work, we apply a technique that enables us to use a contact angle goniometer (24) as a quantitative structural probe by making contact angle measurements with a number of polar and non-polar liquids on feathers that have been dipcoated with a low surface energy coating employed in our past work (25). From these measurements, we self-consistently estimate the spacing ratio characterizing feather structures. This systematic approach also enables us to verify the consistency of the various models used to estimate breakthrough pressures and to rationalize the diving behavior of different bird species. Finally, we use a thermodynamic analysis that reveals the global stability of the Cassie-Baxter non-wetting state on feathers immersed in water and thus connects the measured values of the spacing ratio, the hydrophobicity of the waxy oil coating and the observed behavior of deep (> 10 m) diving birds.

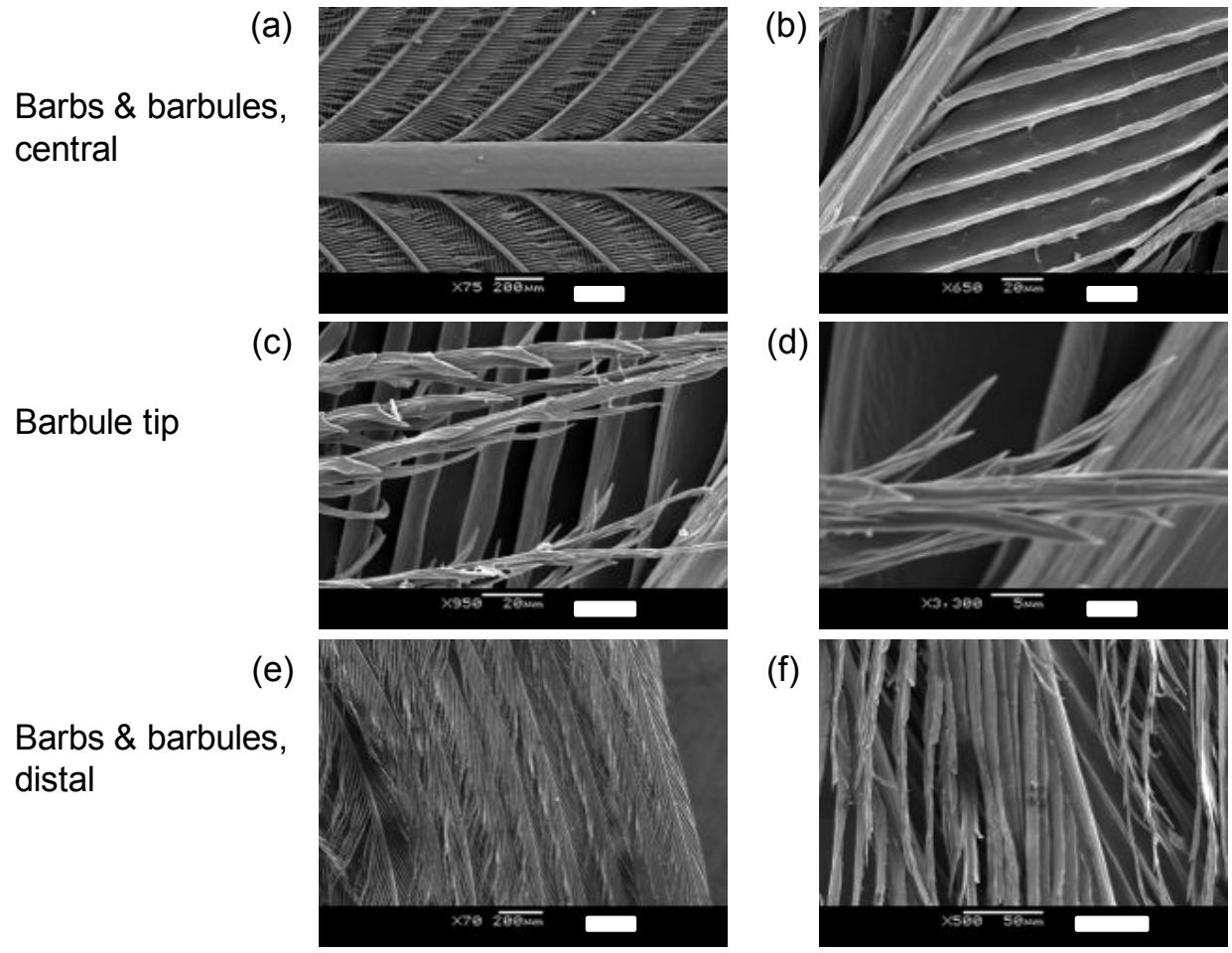

Figure 2. Scanning electron micrographs of the topography of a wing feather of a Common Shelduck are shown. Pairs of images at different magnifications for the central, tip and distal parts of the feather indicate the complexity and hierarchical nature of its texture.

1.1.A wetting-based surface characterization of bird feathers

Feather structures are 'quasi-hierarchical'(17) and involve multiple distinct characteristic length scales, as shown in Figure 2 for wing feathers of the Common Shelduck (*Tadorna tadorna*). The generic features of feathers consist of a main shaft (*rachis*), barbs (*ramus*) that branch out of the main shaft, and barbules that extend from the barbs and often form interlocking microstructures. The feathers are coated by preening oils secreted from the uropygial glands of aquatic birds. These oils are typically hydrophobic and consist of a mixture of waxes, esters and fatty acids that determine the surface chemistry of the bird feathers (21, 26). On a smooth, chemically

homogeneous surface, a liquid droplet exhibits a contact angle at equilibrium (θ_E) given by Young's relation $\cos\theta_E = (\gamma_{sv} - \gamma_{sl})/\gamma_{lv}$, where γ is the pair-wise interfacial tension between the solid (s), liquid (l) and vapor (v) phases respectively (27). Rijke (12) reports an advancing water contact angle (θ^{adv}) on a smooth flat surface comprising of this waxy coating of approximately 90°. Elowson (18) measured values of θ^{adv} on the central primary rachises of the feathers of the African Darter as $\theta^{adv} = 95^{\circ}$ and Mallard as $\theta^{adv} = 88^{\circ}$, again indicating the intrinsic hydrophobicity of the waxy coating on aquatic birds.

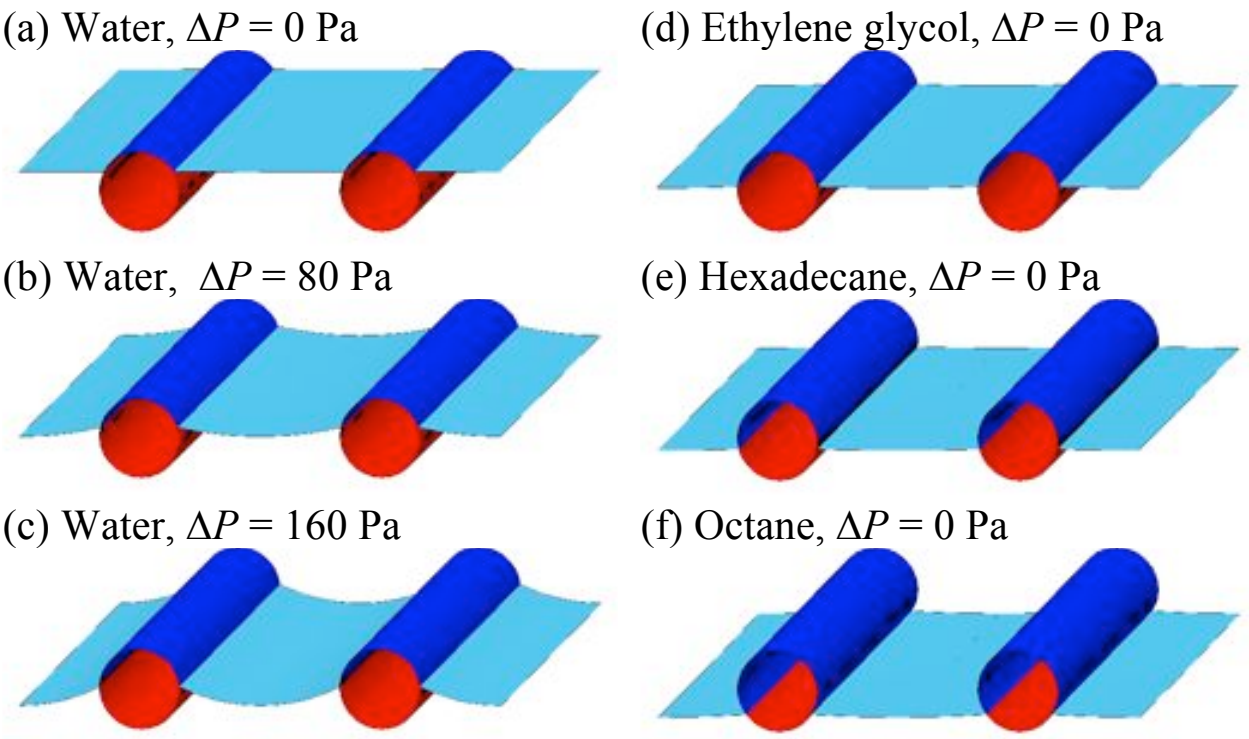

Figure 3. A Surface Evolver simulation of the wetting phenomena of a bird feather by liquids is shown (28). As the pressure differential across the air-water interface increases from (a) zero, (b) 80 Pa, and (c) 160 Pa, higher and higher fraction of the solid texture is wetted by water. The response of the same feather in contact with (d) ethylene glycol (γ_{lv} = 44 mN/m, θ_{adv} = 100°), (e) hexadecane (γ_{lv} = 27.5 mN/m, θ_{adv} = 80°), and (f) octane droplet (γ_{lv} = 21.6 mN/m, θ_{adv} = 60°) with negligibly small pressure differential is depicted.

On rough surfaces, liquid droplets can exhibit one of the following two states – (i) either a composite (Cassie-Baxter) state where the droplets partially rest on the solid elements and partially on the trapped air pockets between the asperities (Figure 1(a)), or (ii) a fully-wetted (Wenzel) state where the droplets wet and penetrate the topography of the surface (29, 30). The topographical details of the feathers are critical in determining whether a bird will maintain the non-wetting Cassie-Baxter state as it dives into water (12, 14, 31). When a hydrostatic pressure differential is applied on the air-water interface (shown in Figure 3(b) to (d)), the contact line moves along the solid textural elements (32). Alternatively, if the surface tension (γ_{lv}) of the contacting liquid is lowered (as shown in Figure 3(e) to (g)) at a fixed pressure differential, the fraction of wetted solid once again increases.

The close correspondence between these two sets of images suggests that probing a feather with water at increasing pressures or immersion depths is analogous to probing the same feather with liquids of successively lower surface tension. We therefore present an approach to quantitatively characterize bird feathers and other textured surfaces by first modifying the surfaces with an ultrathin conformal low energy coating that amplifies the natural liquid repellency and then performing contact angle measurements using a set of probing liquids. In this study, we focus primarily on wing feathers, as those are most relevant during diving and wing spreading phenomena. From these data, we extract an effective spacing ratio and a characteristic length scale of the critical flaws or defects in these complex structures (see Figure 1b). These parameters completely characterize the important wetting aspects of the feather texture. Finally, we seek to elucidate correlations between the details of feather texture and the behavioral response of these birds.

2. Experimental Procedure

2.1. Collection of bird feathers

The wing feathers are obtained from six different species of aquatic birds, three from the same *Phalacrocoracidae* family: the Reed Cormorant, the Great Cormorant, and the European Shag. The remaining species each come from distinct families and were chosen because of their diving and wing-spreading behavior and include: the African Darter, the Common Shelduck, and the

Mallard. Feather samples from twelve birds (two from each species) were furnished by the Natural History Museum (NHM), London, UK. No birds were sacrificed specifically for this study. After pruning, wing, breast, and belly feathers of these birds were selected and representative samples are shown in Figure 4. The wing feathers were chosen for wettability characterization in this work to be representative of the bird plumage, and liquid droplets were deposited on inner and outer vanes for measurement of contact angles.

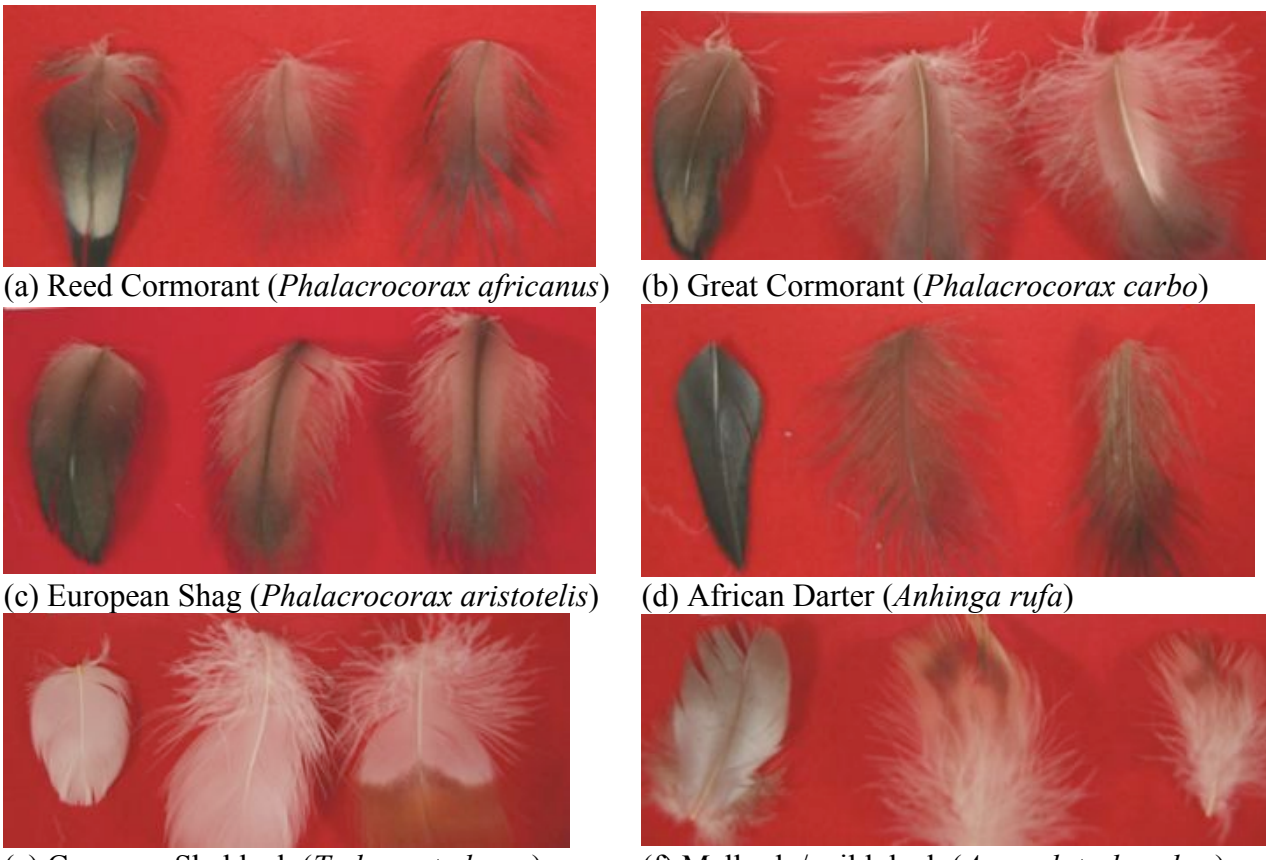

(a) Reed Cormorant (*Phalacrocorax africanus*) (b) Great Cormorant (*Phalacrocorax carbo*)

(c) European Shag (*Phalacrocorax aristotelis*) (d) African Darter (*Anhinga rufa*)

(c) Common Shelduck (*Tadorna tadorna*) (f) Mallard / wild duck (*Anas platyrhynchos*)

Figure 4. Optical photographs of wing, breast, and belly feathers for the six bird species - **(a)** Reed Cormorant, **(b)** Great Cormorant, **(c)** European Shag, **(d)** African Darter, **(e)** Common Shelduck, and **(f)** Mallard are shown respectively. Feathers are typically 2 to 3 cm in length and wing feathers (leftmost among the three feathers) are typically more regular than breast and belly feathers (middle and right feather respectively).

2.2. Coating protocol

Fluorodecyl POSS (polyhedral oligomeric silsesquioxane) molecules consist of silsesquioxane cages surrounded by eight 1*H*,1*H*,2*H*,2*H*-heptadecafluorodecyl groups (33). Due to the high density of perfluorinated carbon atoms, a smooth fluorodecyl POSS surface has one of the lowest solid-surface energy values reported to date ($\gamma_{sv} \approx 10$ mN/m) (34). The very low surface energy of POSS makes it an ideal material for conferring ultrathin, perfectly conformal coatings on topographically complex structures down to the submicrometer length scale (25). Building on our earlier experience with woven fabrics and meshes, we were able to coat the feathers with thin, uniform, flexible, and conformal layer of fluorodecyl POSS mixed with a commercially available fluoroelastomer (Tecnoflon® BR 9151, Solvay Solexis, $\gamma_{sv} \approx 18$ mN/m). Asahiklin AK225 (Asahi Glass Company) was used as the common solvent for the fluorodecyl POSS and Tecnoflon. SEM analysis of images such as Figure 2 before and after coating showed that the Asahiklin solvent did not damage the feather texture. We provide further details of the coating procedure, sample preparation for microscopy and elemental fluorine maps verifying a conformal coating in the Supporting Information (SI).

3. Results and Discussion

A wing feather of a Common Shelduck is moderately hydrophobic in the uncoated state and water droplets ($\gamma_{lv} = 72.1$ mN/m) have macroscopic advancing contact angles of $\theta^*_{adv} = 134 \pm 1^\circ$ (see Figure E1 in SI). However, when probed with lower surface tension liquids like hexadecane or dodecane, the Shelduck wing feather is instantaneously wetted. We can confer enhanced repellency to these low surface tension liquids by dipcoating the feather with the 50:50 mixture of POSS and Tecnoflon. This now enables us to perform contact angle measurements using liquids with decreasing surface tensions and forms the basis for an alternative probing technique to quantify the texture and wettability of feathers. A water droplet on a dipcoated common shelduck feather touches only the uppermost regions of the texture (as indicated by the region colored dark blue in Figure 3(b)). Because the fraction of solid-liquid interface is small, relatively large apparent contact angles are observed. As we sequentially decrease liquid surface tension, from water (Figure 3 (b)) to alkanes like hexadecane (Figure 3 (f)), a higher wetted fraction of the periodic texture is probed. In Table E2 in the SI, we provide the apparent

advancing (θ^*_{adv}) and receding (θ^*_{rec}) contact angles of liquid droplets on the wing feathers of each of the six bird species. The advancing and receding contact angles (θ_{adv} and θ_{rec}) on a perfectly flat, fluorodecyl-POSS-coated surface are also provided for comparison.

The apparent contact angles in the composite (Cassie-Baxter) state decrease with decreasing surface tension (γ_{lv}) and below a threshold value, the droplets irreversibly transition from a composite non-wetting state and spread rapidly across the structure to establish a wetted state with a much lower apparent contact angle. For example, a liquid drop of hexadecane ($\gamma_{lv} = 27.5$ mN/m) exhibits an apparent contact angle of $\theta^*_{adv} = 97 \pm 5^\circ$ on a dip-coated feather of the African Darter. However, a drop of dodecane ($\gamma_{lv} = 25.3$ mN/m) placed on the same dip-coated feather immediately transitions to the fully-wetted state and spreads across the feather resulting in an apparent contact angle of $\theta^*_{adv} = 0^\circ$.

The quasi-hierarchical structure of the feather (17) implies that there are multiple length scales accessible to the liquid drop as it probes the topography of the feather. Because the non-wetting Cassie-Baxter state for low surface tension liquids on the dip-coated feathers is metastable, a single defect site on the feather can act locally as a nucleation center that induces a local transition to the Wenzel state, which then propagates to the rest of the feather. This nucleation and subsequent propagation of the metastable Cassie-Baxter to Wenzel transition on the dip-coated feathers is specific to low surface tension liquids (with values of $\theta_E < 90^\circ$). A similar wetting transition at the defect sites is not observed for water ($\theta_E = 124^\circ$) and the transition to the Wenzel state is instead determined by the smallest length scale (i.e., barbules) of the structure as we show in section 3.3.

As we describe below, the goniometric measurements of $\left\{\theta^*_{adv}, \theta_{adv}\right\}$ (provided in Table E2 in SI) allows us to:

(i) Provide a wetting-based quantification of D^*, the effective cylinder spacing ratio of the feathers that was investigated by Rijke (12);

(ii) Predict the hydrostatic breakthrough pressure (P_b) for each feather structure;

(iii) Estimate ℓ_{defect}, the characteristic length-scale of defects that governs the Wenzel transition for droplets of low surface tension liquids.

Within this global framework, the contact angle data characterize the average topographical details, and allow us to use wetting as a 'goniometric microscope' (34).

3.1. Characterization of feathers using advancing contact angles and a dimensionless spacing ratio

We use a 1-D cylindrical framework to model the wettability of the feathers. The apparent macroscopic contact angle is related to the topography of the feathers and the coating chemistry by the Cassie-Baxter relation, which can be expressed for this model as (18):

$$\cos\theta^*_{adv} = -1 + \frac{1}{D^*}\left[(\pi - \theta_{adv})\cos\theta_{adv} + \sin\theta_{adv}\right] \quad (1)$$

Here, θ^*_{adv} represents the measured macroscopic apparent contact angle, θ_{adv} is the measured advancing value of the contact angle on a flat, fluorodecyl-POSS-coated surface and $D^* = (R+D)/R$ is a dimensionless geometric parameter defined in terms of the cylinder radius (R) and half-spacing (D). The cosine values of the apparent advancing contact angles measured on the coated feathers are plotted against the cosine of advancing contact angles (θ_{adv}) measured on chemically-identical, but smooth spin-coated silicon wafer surfaces, as shown in Figure 5 for the six bird species under investigation. Using the Cassie-Baxter (CB) relation for a cylindrical texture (Equation 1), a non-linear regression was performed with D^* as the only regression parameter (the solid curve). A 95% confidence interval is used as a metric of uncertainty for the value of the spacing ratio D^* (the two dashed lines in Figure 5, values listed in Table 1). The spacing ratio characterizing the wing feather is denoted D^*_{eff} and was found to be significantly different for the various birds, ranging from a value as low as D^*_{eff} =1.28 for the African Darter to as high as D^*_{eff} =1.91 for the European Shag (Table 1).

Estimating an appropriate value of this geometric spacing ratio (D^*) using micrographs (such as those in Figure 2) is difficult due to the complexity of the feather structures. As a result, there are conflicting reports in the literature of the values of D^* obtained from microscopy on barbs and barbules (henceforth denoted $D^*_{microscopy}$). In Table 1, we list the effective values of the spacing ratio we obtain from fitting to contact angle data (Figure 5), alongside values of $D^*_{microscopy}$ from the early work of Rijke (12) on breast feathers and subsequent work of Elowson (18) on breast and wing feathers. A comparison between the two columns indicates that our small values of $1 < D^*_{eff} < 2$ are consistent with Elowson's microscopy-based estimates at the barbule scale of wing feathers. In the following sections we demonstrate that the values of D^* obtained from the wetting of the barbules and the analysis shown in Figure 5 are consistent with the overall observed wetting, de-wetting, and breakthrough pressure of typical wing feathers whereas the larger literature values of $D^*_{microscopy}$ (corresponding to barbs) lead to erroneous predictions.

Table 1. Effective values of the spacing ratio (D^*_{eff}) measured on wing feathers from the present work are compared against values obtained from microscopy ($D^*_{microscopy}$) of barbs and barbules from the literature for wing feathers (second column) and breast feathers (third column). In the last column, an estimate of the half-spacing of defect sites (ℓ_{defect}) deduced from contact angle measurements is also reported, and its significance is detailed in Section 3.5 in the main text.

Bird species	D^*_{eff} Wing Feathers	$D^*_{microscopy}$ Wing Feathers		$D^*_{microscopy}$ Breast Feathers		ℓ_{defect} (μm)
		Barbs	Barbules	Barbs	Barbules	
African darter	1.28 ± 0.1	1.7 [a]	1.6 [a]	4.5 [b], 9.9 [a]	7.6 [a]	220 ± 50
Reed cormorant	1.24 ± 0.14	4.2 [a]	2.4 [a]	4.3 [b], 8.5 [a]	2.9 [a]	190 ± 70
Great cormorant	1.57 ± 0.15	--		4.8 [c]	--	290 ± 30
Mallard	1.84 ± 0.13	5.7 [a]	1.9 [a]	5.9 [b], 10.6 [a]	2.9 [a]	250 ± 30
European shag	1.91 ± 0.16	--	--	--	--	350 ± 30
Common shelduck	1.89 ± 0.12	6.7 [a]	2.1 [a]	11.1 [a]	3.5 [a]	280 ± 30

[a] Elowson (The Auk, 1984); [b] Rijke (J. Exp. Biol., 1968);

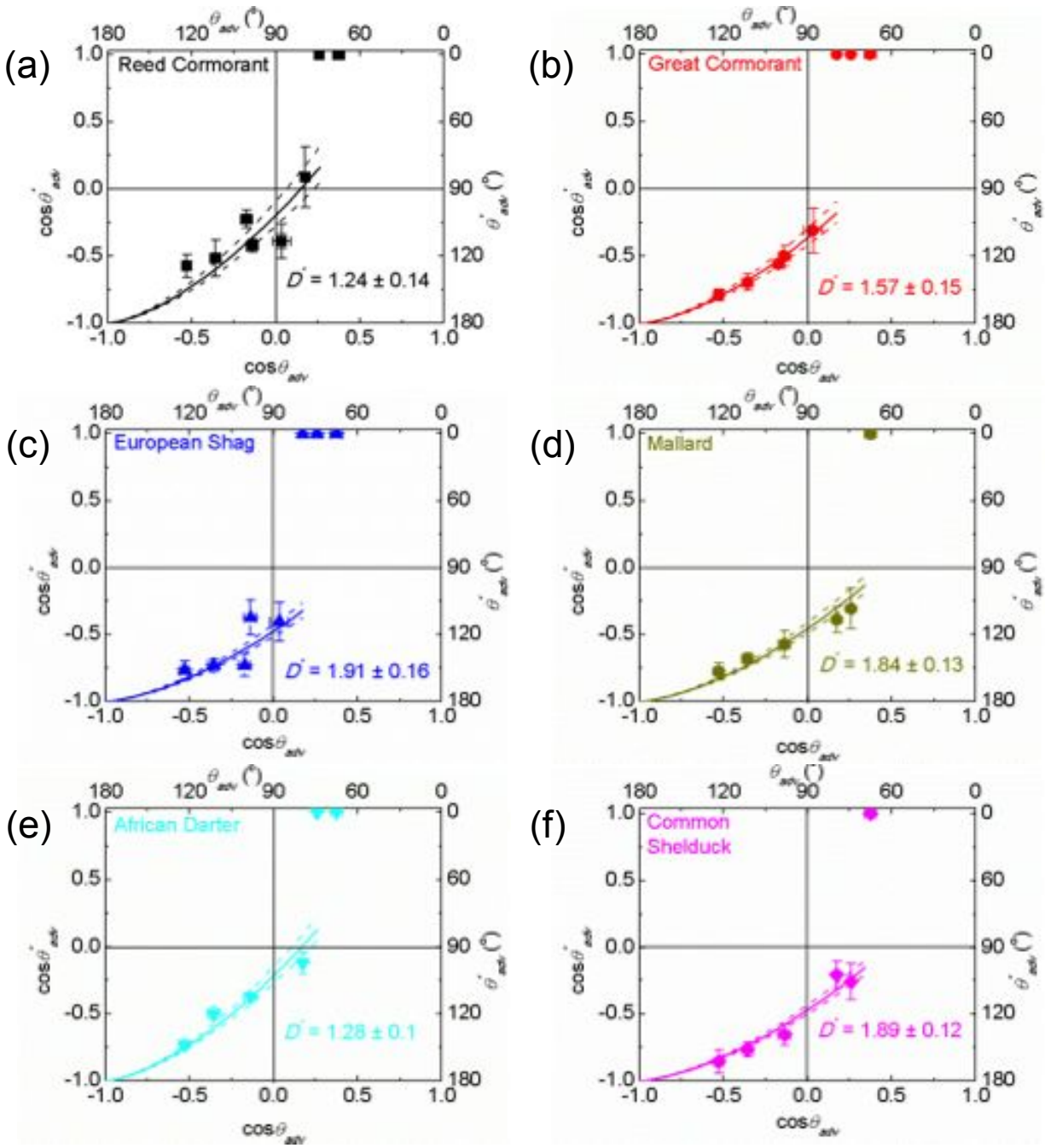

Figure 5. Apparent advancing contact angles (θ^*_{adv}) of various liquids on fluorodecyl POSS / Tecnoflon coated feathers and on smooth silicon wafers spin-coated with the same coating (θ_{adv}) are plotted for the six bird species. Values of the effective spacing ratio (D^*_{eff}) extracted from a best fit to the Cassie-Baxter theory (solid lines; Eqn 1) are also indicated, along with 95% confidence intervals (dashed lines).

3.2. Predicting breakthrough pressures of water on feathers

The preceding structural analysis utilized the Cassie-Baxter relation (Equation 1) to obtain a goniometric measure of the dimensionless spacing ratio (D^*) on the feathers, which we can then use in turn to predict the breakthrough pressure of water for each bird species. As the bird dives underwater, a pressure differential $\Delta P = \rho g h$ builds up across the composite air-liquid interface. As a result, the interface must become curved to sustain this pressure differential. In Figure 6, we show an illustration of the liquid meniscus between parallel cylinders of radius R and half-spacing D under the influence of a dimensionless pressure differential $\hat{P} = \Delta P / \left(2\gamma_{lv} / R\right)$. The position of the contact line is characterized by the angle ϑ subtended between the contact line and the vertical line through the center of the cylinder. In the absence of an external pressure differential $\left(\Delta P = 0\right)$, the liquid/air meniscus is flat, and is located at $\vartheta = \theta_E$. For $\Delta P > 0$, the position of the contact line on the cylinder is determined by a balance of the capillary force and the pressure force as detailed in the supporting information. Beyond a certain threshold, a transition to the fully-wetted (Wenzel) state can occur by either a depinning, sagging or coalescence mechanism (35). Determining which of the various modes of failure occurs first involves both knowledge of the geometry as well as making specific assumptions about the model that represents the barbs and barbules of the feathers. Bormashenko (17) developed an analytical expression for the pressure differential at which a depinning transition occurs on a single layer of freely suspended parallel cylinders. As we show explicitly in the SI, this depinning transition requires $D^* < \left|\tan\theta_E\right|$. Therefore, if the barbules are spaced widely apart, this depinning transition does not occur. In the absence of this transition, Bormashenko assumes the liquid meniscus transitions to the fully-wetted state only when it coalesces around the cylinder. However, the dense underlying structure on a feather (as seen in Figure 2b), can also permit a sufficiently curved liquid meniscus to interact with additional underlying layers of solid features leading to a Wenzel transition. We can describe this possibility by also allowing for a 'sagging' transition (in place of Bormashenko's coalescence transition) resulting from meniscus contact with an underlying planar solid substrate (i.e., $h \to 0$ in Figure 6). This allows us to combine Bormashenko's results on the depinning transition with independent calculations of the

sagging transition to obtain a single framework for determining the breakthrough pressure (P_b) according to Equation SI-8 in the supporting information. We also provide a state space plot (Figure F3 in the SI) to indicate the actual mode of transition for various pairs of $\{D^*, \theta_E\}$.

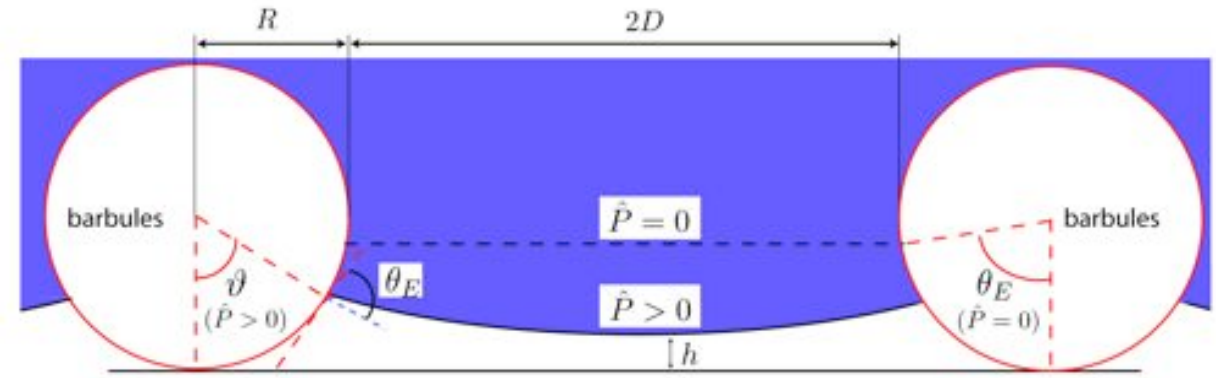

Figure 6. Schematic of the Cassie-Baxter composite interface resting on an array of parallel barbules of radius *R* and half spacing *D* and under a dimensionless external pressure differential $\hat{P} = \Delta P / P_{ref}$ where $P_{ref} = 2\gamma_{lv} / R$. Here, θ_E is the equilibrium contact angle of the liquid, ϑ is the angular coordinate characterizing the location of the contact line and h is the altitude of the bottom of the curved meniscus above the substrate. The horizontal dashed line indicates the location of the meniscus in the absence of any external pressure differential.

As expected (cf. Equation SI-8), the critical pressure for breakthrough P_b is inversely proportional to the length scale of the texture (*R*) and therefore the selection of *R* is critical in the design of robust non-wetting textures. In a typical bird feather, there are many different length scales corresponding to the barb, barbules, and tiny offshoots from the barbules. Because barbules occupy most of the area fraction of the feather, the length scale of these barbules is expected to be the dominant length scale. Motivated by the scanning electron micrographs in Figure 2(a-f), and the data of Elowson(18), we select a typical value of the barbule length scale of $R \sim 5\mu m$. We also use the advancing contact angle (θ_{adv}) in lieu of the equilibrium contact angle (θ_E) to account for inhomogeneities on the surface of the feather (36). Therefore, this

value of R allows us to predict the breakthrough pressure of water (P_b) by using Equation SI-8, along with knowledge of D_{eff}^{*} and θ_{adv} for the feathers of the various bird species.

Table 2. Critical angular location (ϑ_c), predicted breakthrough pressure for water droplets (P_b) and the corresponding transition mode are compiled for the uncoated wing feathers of the six bird species. The last three columns contain empirically observed diving depth, diving speed and wing-spreading behavior for the same bird species.

Bird species	Critical Angular Location (ϑ_c°)	Predicted Breakthrough Pressure, P_b (kPa)	Predicted Transition mode	Diving depth (m)	Diving speed (m s^{-1})	Wing-spreading
African darter	68	28	Depinning	< 5	0.19 ± 0.16[†]	Y
Reed cormorant	73	40	Depinning	5 – 6[*]	0.7 – 0.85	Y
Great cormorant	62	19	Depinning	4.7, < 10[‡]	1.1-2.1	Y
Mallard	57	13	Sagging	Dabbling	Dabbling	N
European shag	58	12	Sagging	33 – 35	1.7-1.9	Y
Common shelduck	61	13	Sagging	Dabbling	Dabbling	N

* from neutral buoyancy experiments, not natural observation; [†] horizontal traveling speed, not diving speed; [‡] usually < 10 m, but can dive to depths of 35 m (37); Wing-spreading: Y = predictably, N = never; Dabbling = dabbling species, not primarily divers.

To obtain the unknown value of θ_{adv} for each feather, we make use of the fact that although our FluoroPOSS coating significantly modifies the intrinsic surface chemistry of the feathers, the thin (< 200 nm) and conformal nature of the coating ensures that the values of the effective spacing ratio (D^{*}) remain the same as the uncoated feather. In addition, apparent advancing contact angles for water droplets (θ_{adv}^{*}) on the uncoated feathers can be measured. Using the CB relation (Equation 1), and the values of θ_{adv}^{*} and D_{eff}^{*} from Figure 5 (and Table E2 in the SI), the desired values of θ_{adv} for water droplets on the inherent waxy coating of the feathers can be calculated (presented in the second column of Table 3). We use these advancing contact angles

in place of the equilibrium contact angles for each feather to determine the breakthrough pressures (P_b) and these values are listed in Table 2.

We observe in Table 2 that the predicted breakthrough pressure for the Cassie to Wenzel transition on the feathers of the various species is in the range of 10 kPa - 40 kPa for all 6 species, which corresponds to a 1 m - 4 m maximum diving depth in water, consistent with the independent estimate obtained by Bormashenko (17). Therefore, from our calculations of the breakthrough pressure, the diving depths at which the non-wetting Cassie state is maintained are towards the lower end of the spectrum of the typical diving depths reported for the African Darter and Reed Cormorant. In addition, for the Great Cormorant and the European Shag, which reach depths of upto 35 m while hunting for fish, our calculations predict that the individual bird feathers will indeed become fully wetted during a typical dive. Using our analysis, the barbules would need to be as small as $R \sim 0.3\mu m$ to achieve diving depths of 35 m while maintaining the non-wetting state, which is inconsistent with the observed structural length scales shown in the scanning electron micrographs in Figure 2. This suggests that evaluating the resistance to meniscus breakthrough is not sufficient by itself to completely explain the diving and wing spreading behavior of deep-diving aquatic birds.

In the SEM image shown in Figure 1(b), we can identify the presence of large defect sites in the feather structure. We can quantify these defect sites by introducing a local effective half-spacing (ℓ_{defect}) on the quasi-hierarchical feather that models the in the observed spreading of low surface tension liquids across the feather structures. These defect sites correspond to the initial nucleation site, which initiates transition to the Wenzel state for the low surface tension liquids. The expression for ℓ_{defect} can be expressed as

$$\ell_{\text{defect}} = \frac{r_{\text{drop}}}{2}\left(D^* - 1\right)\left(\frac{\sin(\theta_{adv} - \vartheta_c)}{D^* - \sin\vartheta_c}\right) \qquad (2)$$
$$\vartheta_c = \max(\vartheta_d, \vartheta_s)$$

where r_{drop} is the radius of the probe liquid drop and ϑ_c is the critical angular location at which the Cassie to Wenzel transition occurs (cf. Section G in the SI). For a wing feather of a Common

Shelduck, we find the defect length scale, $\ell_{\text{defect}} = 280\,\mu\text{m}$. The same exercise is repeated for the wing feathers of other five bird species and the results are summarized in the last column of Table 1. All six bird species have similar values of the half-spacing of defect sites ($\ell_{\text{defect}} \sim 200\mu\text{m} - 300\mu\text{m}$). These values of the defect length scale are much larger than the barb or barbules length scale ($\ell_{\text{defect}} >> D$), highlighting the quasi-hierarchical structure of the feather. The scale of the defects suggest that the Cassie-Wenzel transition for low surface tension metastable liquids is controlled by topographic features that are an order of magnitude larger than those typically considered in optical microscopy of the feather.

In summary, the overall wetting behavior of the wing feathers of each of the six bird species has been characterized in terms of two structural parameters – (1) an effective spacing ratio (D^*_{eff}) that governs the breakthrough pressure required to disrupt the non-wetting water/air interface on the smallest features on the feathers (i.e., the barbules with $R \sim 5\mu\text{m}$) and (2) a larger defect length scale ℓ_{defect} that governs the breakthrough of the metastable composite interface formed with low surface tension liquids. The difference between the characteristic length scales that govern the breakthrough of the composite interface with water, as opposed to low surface tension liquids, arises from the global thermodynamic stability of the non-wetting CB state formed with water when the equilibrium contact angle is above a certain critical contact angle, as we now proceed to show.

3.3. Surface Energies of Cassie-Baxter (CB) and Wenzel state interfaces

An expression for the surface energy of the composite CB interface relative to an initial reference state can be obtained for the array of parallel cylinders. The reference state is the initial planar interface that exists in the absence of a pressure differential (i.e, $\hat{P} = 0; \vartheta = \theta_E$). The total surface energy is the sum of two terms: (1) the evolving solid/air and solid/liquid interactions that accrue as the contact line descends along the barbule (governed by the Young–Dupré equation), and (2) the incremental energy of the increasing liquid/air interface resulting from the curvature of the meniscus. In the supporting information, we derive the following expressions for

the surface energies for the CB state (ΔE_C) and the Wenzel state (ΔE_w) relative to the initial reference state:

$$\frac{\Delta E_{CB}}{2RL\gamma_{lv}} = -(\theta_E - \vartheta)\cos\theta_E + \left[\frac{(\theta_E - \vartheta)(D^* - \sin\vartheta)}{\sin(\theta_E - \vartheta)} - (D^* - \sin\theta_E)\right]$$
$$\frac{\Delta E_W}{2RL\gamma_{lv}} = -\theta_E\cos\theta_E - (D^* - \sin\theta_E) - D^*\cos\theta_E \quad (3)$$

The surface energy is scaled by a reference energy $2RL\gamma_{lv}$, where L is the length of the cylindrical element. The final term in the expression for the energy of the Wenzel state is introduced to account for the interactions on the underlying flat substrate. In Figure 7, we show the free energy of the interface on an array of cylindrical barbules as it evolves with increasing applied pressure differential for a fixed value of $D^* = 1.5$, and for two values of equilibrium contact angles of $\theta_E = 120^\circ$ and $\theta_E = 60^\circ$ (representative of the behavior of water and oils). The solid line corresponds to the surface energy of the CB state (ΔE_{CB}), and the dashed line is the energy of the fully-wetted Wenzel state (ΔE_W), determined from Equation 3. For both curves, the initial equilibrium non-wetting reference state A (i.e., $\hat{P} = 0; \vartheta = \theta_E$) is located at a local minimum of the surface energy. The surface energy of the composite interface increases with increasing external pressure differential as the meniscus descends along the cylindrical features. When $\theta_E = 120^\circ$ and $D^* = 1.5$ (blue curve), the liquid meniscus transitions to the Wenzel state by a depinning mechanism, indicated by state B ($\hat{P}_d = 0.69; \vartheta_d = 65^\circ$) in Figure 7. Beyond this point $d\hat{P}/d\vartheta > 0$ and the interface is mechanically unstable. The dimensionless surface energy just before this transition occurs is $\Delta E_c/(2\gamma_{lv}RL) = 0.54$. The numerical value of the surface energy at the transition state can be interpreted as an energy barrier that must be overcome before transition. Further, we observe that when $\theta_E = 120^\circ$ and $D^* = 1.5$, the final fully wetted Wenzel state (dashed line) is at a higher energy ($\Delta E_w/(2\gamma_{lv}RL) = 1.16$) than the transition state B. This indicates that the globally stable equilibrium state is the CB non-wetting state; therefore upon

decreasing the external pressure differential, the Wenzel state will spontaneously dewet and re-establish the composite non-wetting CB interface.

By contrast, the wetting behavior of an oil (green curve; $\theta_E = 60^\circ$) on the cylindrical features with the same structural spacing ratio ($D^* = 1.5$) is markedly different. The surface energy once again increases from the initial reference state A'. However in this case, the meniscus transitions to the Wenzel state by a sagging mechanism, indicated by State C' ($\hat{P}_s = 0.22; \vartheta_s = 36^\circ$). The dimensionless surface energy barrier just prior to transition is only $\Delta E_c / (2\gamma_{lv} RL) = 0.09$, much smaller than the corresponding transition value obtained for water. The most characteristic feature of the wetting of the oil is the much lower energy of the Wenzel state ($\Delta E_w / (2\gamma_{lv} RL) = -1.9$) relative to both the transition state C' and the initial state A'. The negative value of the surface energy for the Wenzel state indicates that the wetting transition is irreversible for this oil, and the liquid will not recover to the initial non-wetting state even upon complete removal of the external pressure differential.

The irreversibility of the wetting transition highlights the metastable nature of the non-wetting state for oils (38, 39), and an estimate of the magnitude of the energy barrier prior to transition is provided by Equation 3. So far, we have considered the wetting energies of two liquids with different values of θ_E on the same structural element. A similar irreversible wetting transition can occur for water by simply increasing the value of the dimensionless spacing (D^*). An understanding of the energetics of wetting, and the global stability of the Cassie-Baxter non-wetting state on the cylindrical elements of the feathers, is therefore essential in interpreting the diving and wing spreading behavior of birds.

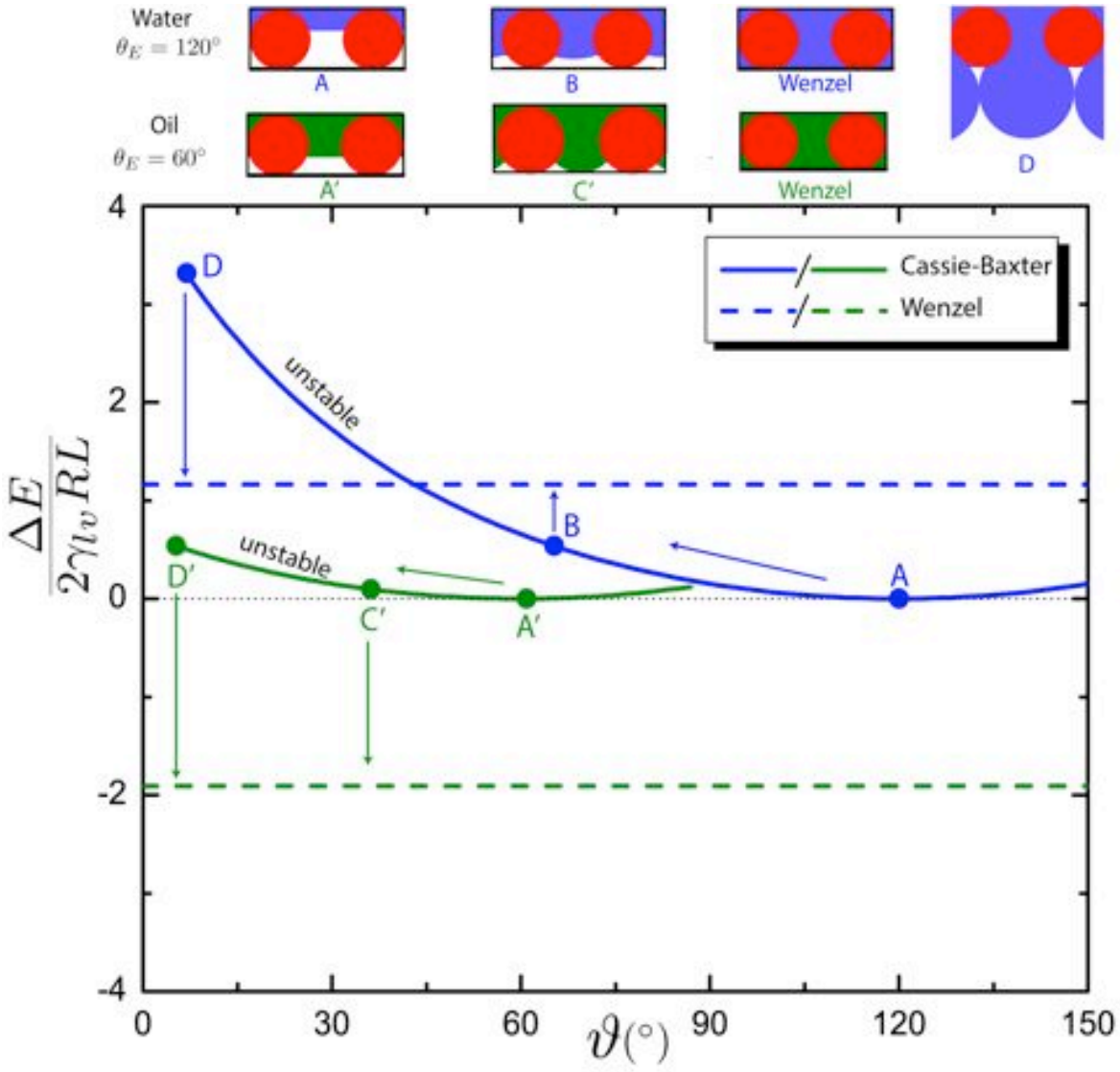

Figure 7. Plot of the total surface energy of the composite solid/liquid system against the angular position ϑ of the interface on a 1D array of parallel cylinders of diameter $2R$, half spacing D with a dimensionless geometric spacing $D^* = (R + D)/R = 1.5$. The solid curves indicate the energies of the composite interface corresponding to the Cassie-Baxter non-wetting state, and the dotted line indicates the surface energy of the fully-wetted Wenzel state. The blue and green curves are evaluated for water ($\theta_E = 120^\circ$) and a typical oil ($\theta_E = 60^\circ$) respectively. A schematic of the liquid meniscus corresponding to the initial state A, depinning transition state B, sagging transition state C and the Wenzel state are shown above the plots. State D is associated with the coalescence transition proposed by Bormashenko, when a rigid, underlying substrate is absent, as shown in the sketch.

3.4. Thermodynamics of wetting – binodal and spinodal

To test whether water droplets on a given bird feather are in a thermodynamically-stable Cassie-Baxter state, values of the contact angle on a smooth surface with identical chemistry (θ_E) are needed. By using the best-fit value of D^* from our goniometric analysis on the dip-coated feather, and measuring the apparent advancing contact angle on each uncoated feather, we can estimate the advancing contact angles on the inherent waxy oil covering natural feathers, as discussed in Section 3.2. We list these values in the second column of Table 3.

Table 3. Critical angle for the Cassie-Baxter to Wenzel transition (θ_c) based on D^* values and estimated values of advancing contact angles (θ_{adv}) for water on the waxy preen oil coating that is present on a feather.

Bird	D^*	Estimated CA θ_{adv} (°)	θ_c (°)
African darter	1.28 ± 0.10	112 ±2	96 ± 2
Reed cormorant	1.24 ± 0.14	118 ± 2	95 ± 3
Great cormorant	1.57 ± 0.15	117 ± 6	100 ± 2
Mallard	1.84 ± 0.13	105 ± 3	104 ± 2
European shag	1.91 ± 0.16	106 ± 3	105 ± 2
Common shelduck	1.89 ± 0.12	116 ± 2	104 ± 1

* Uncertainty in θ_{adv} is computed using Monte Carlo simulation with 10,000 repeats and by sampling values of D^* and θ^* as random normal distributions.

On a wetting surface ($\theta_E < 90°$), the fully-wetted state represents the global equilibrium state with minimum free energy, whereas on a strongly non-wetting surface ($\theta_E >> 90°$), the composite solid-liquid-air interface is the global equilibrium. The thermodynamic crossover condition between the two states is analogous to a binodal transition (40) that can be found by equating the two expressions (Cassie-Baxter and Wenzel) for apparent contact angles to give

$$D^* = \frac{\sin\theta_C - \theta_C \cos\theta_C}{1 + \cos\theta_C} \tag{4}$$

These critical values are shown as the last column in Table 3 and are plotted as the broken line in Figure 8.

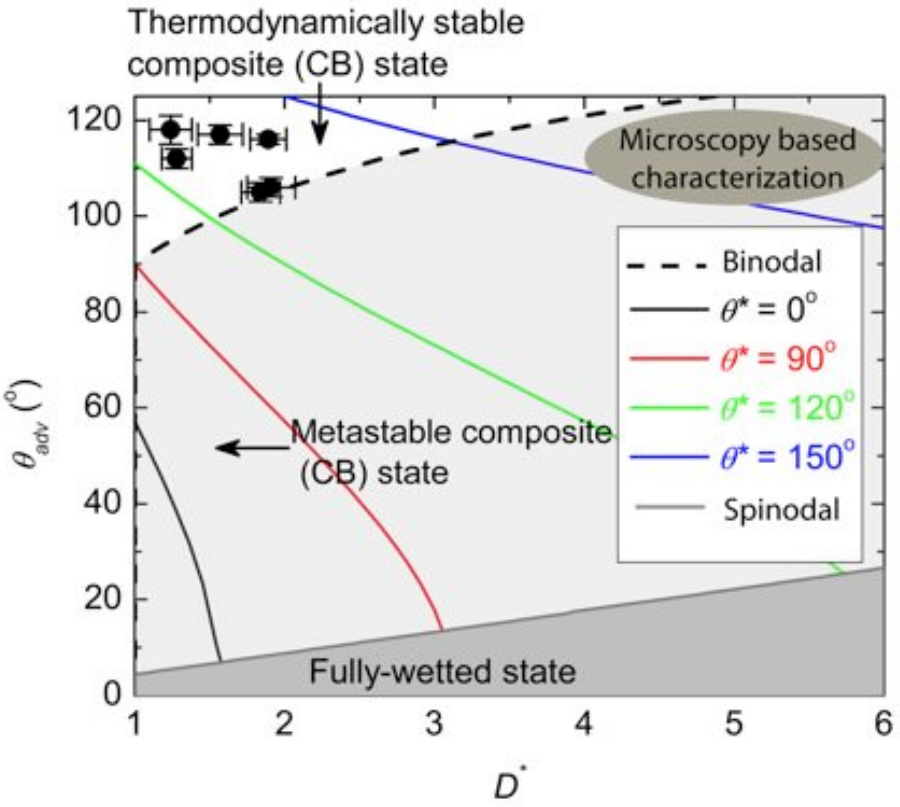

Figure 8. A phase diagram of surface wettability is plotted with advancing contact angles (θ_{adv}) on the ordinate and a best-fit value of the effective spacing ratio (D^*) on the abscissa. Isocontours of constant apparent contact angle (evaluated using Equation 1) are shown by solid colored lines. The dashed line corresponds to the binodal line (Equation 4) separating the thermodynamically stable Cassie-Baxter states and the metastable Cassie-Baxter states (light grey). The water contact angle data for the 6 bird species under consideration all lie *above* the binodal where the composite interface is the equilibrium state. The metastable region of the chart below the binodal (light grey) is obtained by equating the Laplace pressure of a water drop with radius equal to its capillary length, to the breakthrough pressure calculated from Equation SI-8 with R = 5 μm. The solid grey line indicates the spinodal. In the region below the spinodal (dark grey) the Cassie-Baxter state is unstable and will undergo a spontaneous transition to the fully-wetted Wenzel state.

This line demarcating the stable and metastable regions in Figure 8 is analogous to a binodal curve and can also be obtained by setting $\Delta E_w = 0$ in Equation 3, when the energy of the fully-wetted Wenzel state is exactly equal to the *lowest energy* of the Cassie-Baxter state (when the pressure difference $\hat{P} = 0$).

If, for a given barbule spacing D^*, the composite interface (or Cassie-Baxter state) is globally the lowest energy state, then it is necessary that $\theta_{adv} > \theta_c$. This corresponds to the region above the binodal in Figure 8. When $\theta_{adv} < \theta_c$, the fully-wetted Wenzel state has a lower free energy than the Cassie-Baxter state. However a liquid droplet on a feather can still be trapped in a metastable non-wetting Cassie-Baxter state beneath the binodal, in the region shaded light grey in Figure 8 until a defect nucleates and grows leading to an irreversible wetting transition. Organic liquids with $\theta_E < 90^\circ$ that produced non-zero contact angles on the coated feathers all lie in this lightly shaded (metstable) region between the binodal and spinodal in Figure 8. Liquid droplets in metastable CB states eventually transition into the more stable Wenzel state under pressure perturbations. From Equation SI-8, the breakthrough pressure (P_b) required depends on the spacing ratio (D^*) and the barbule length scale (R). The dark grey region in Figure 8 below the spinodal curve indicates the region where the transition to the thermodynamically-stable fully-wetted Wenzel transition state is spontaneous, and the non-wetting Cassie-Baxter state is thermodynamically unstable. A representative spinodal curve, evaluated with a barbule length scale of R = 5 μm is plotted as the dark grey line in Figure 8, where the characteristic length scale of the Laplace pressure for a large drop corresponds to the capillary length of water ($r_{drop} = 1.7$ mm).

On comparing the last two columns of Table 3, it is clear that for all six bird species, the value of the advancing contact ($\theta_{adv} \sim$ 105-118°) that we compute for each feather (by using the best-fit value of D^* obtained from our goniometric analysis) is larger than the corresponding critical contact angle θ_c (*i.e,* $\theta_{adv} > \theta_c$). Therefore, based on our goniometric analysis, we conclude that water droplets sitting on the quasi-hierarchical feathers of all six birds are infact, in a thermodynamically-stable Cassie-Baxter state, as shown in Figure 8. The wetting behavior of the natural waxy coating (or preen oil) on aquatic bird feathers that we estimate is, at best, moderately hydrophobic ($\theta_{adv} \sim$ 105-118°), and therefore a low value of the effective spacing ratio between barbules ($1 < D^* < 2$) is essential to push the feathers above the binodal (dashed line) in Figure 8. Various microscopy-based estimations reported in the literature (12, 14, 18-20, 22), particularly those based on barb dimensions, lead to much larger values of the spacing ratio

($D^* \approx 3 - 10$). This would erroneously locate the feathers in the top right corner of Figure 8, in a region where the fully-wetted Wenzel state is the global equilibrium for water-feather interactions.

3.5. Connection between wetting, thermodynamics and avian diving

Based on our analysis, the predicted breakthrough pressure for feathers is toward the lower end of the typical hydrostatic pressure that the feathers are subjected to in a dive. With increasing hydrostatic pressure, the air between the barbs and barbules is gradually replaced by water as the air-water interface bulges (see Figure 3). Therefore, the individual feathers are expected to ultimately be fully-wetted in a typical dive.

However, as the birds return to the surface, this Wenzel state becomes energetically unfavorable compared to the solid-liquid-air composite state. Drainage induced de-wetting of the texture is expected, but this energetically favorable transition behavior may be retarded by kinetic barriers that trap some of the water temporarily in the feather texture. Spreading of the wings will help to facilitate the transition from the Wenzel to the Cassie-Baxter state by reducing contact line pinning of droplets. The rate of transition from a fully-wetted state to a composite state will depend on the geometry and wetting characteristics of the feather (e.g., the barb spacing and the advancing contact angle). However, for the feathers of all six aquatic birds under consideration here, our goniometric analysis suggests that the non-wetting state is thermodynamically favorable. In contrast to the six aquatic species studied here, Bormashenko (30) has determined the equilibrium contact angle of water on the central rachis of pigeon feathers to be $\theta_E = 72^\circ$ (i.e, the pigeon feather is mildly hydrophilic). Therefore, our framework implies that although pigeon feathers repel water, the corresponding Cassie-Baxter state with water is, at best, metastable. The enhanced hydrophobicity of the waxy coating and preening oil employed by aquatic diving birds ($\theta_E > 90^\circ$) coupled with low values of D^* are essential for the feather to spontaneously dewet after each dive.

4. Conclusions

In this work, we have extended and applied our understanding of the wetting of fibrous textured surfaces to bird feathers. From the thermodynamic analysis we show that a combination of the structural details of the feathers (i.e, densely spaced barbules with low values of D^*) along with the hydrophobic surface chemistry (i.e, $\theta_E > 90^\circ$) together can help establish the Cassie-Baxter composite state as the global equilibrium state when feathers are in contact with water. By contrast, for lower surface tension liquids or widely spaced barbules, this Cassie-Baxter state is, at best, metastable. The characteristic length scale of the barbules determined from microscopy ($R \sim 5\mu m$) sets the breakthrough pressure for the case of water, while the much larger defect length scale (ℓ_{defect}) controls the loss of metastability for droplets of organic liquids placed on the same feather structures.

The estimated hydrostatic breakthrough pressures of water on the textures of all six wing feathers indicated that individual feathers are expected to become wet at moderate depths, on the order of a few meters, smaller than the typical diving depths attained by the African Darter, Reed Cormorant and the European Shag. Using our dipcoating approach, we are able to locate the various feather textures on a wetting state phase diagram and thereby show that a non-wetted solid-liquid-air composite interface is the global equilibrium state of water droplets on these feathers at atmospheric pressure. Once the birds emerge out of water, the dewetting transition is thermodynamically favorable. The wing spreading behavior demonstrated by these species might help facilitate this dewetting/water-shedding if there are pinning sites or other kinetic traps that delay the spontaneous drying of feathers and their return to the lowest energy Cassie-Baxter state.

We have also demonstrated that feathers of aquatic bird species with a thin, conformal POSS/Tecnoflon omniphobic coating are not wetted by low surface tension liquids like hexadecane and dodecane. From measurements of the apparent advancing contact angle data (θ^*_{adv}) on the dip-coated feathers, we extracted a dimensionless spacing ratio ($1 < D^* < 2$) and a measure of the half-spacing of defect sites ($190\mu\text{m} < \ell_{\text{defect}} < 350\mu\text{m}$) that characterize the quasi-

hierarchical structure of each bird species. These two structural parameters capture the most important wetting aspects of the complicated texture of bird feathers in terms of a simple 1-D cylindrical model. This approach provides a simple and quantitative method to investigate bird feathers, compared to previous work based on microscopic or photographic evaluation. Applying this systematic and self-consistent framework to measurements on feathers of other avian species will help to correlate the structure of bird feathers with observed aquatic behavior.

5. Acknowledgements

The authors acknowledge financial support from the Army Research Office (ARO), the Office of Naval Research (ONR) and the MIT-Legatum Center for Development and Entrepreneurship. The authors also thank the Center for Materials Science and Engineering and the Institute of Soldier Nanotechnologies at MIT for the use of experimental facilities and Mr. Justin Kleingartner for helpful discussion during the preparation of the manuscript.

6. References

1. Salibian A, Montalti D. 2009 Physiological and biochemical aspects of the avian uropygial gland. *Braz J Biol*. **69**,437-446.(doi:10.1590/S1519-69842009000200029)
2. Brocher F. 1912 Recherches sur la respiration des insectes aquatiques adultes. *Les Haemonia. Ann. Biol. Lacustre*. **5**,5-26
3. Thorpe WH. 1950 Plastron Respiration in Aquatic Insects. *Biological Reviews*. **25**,344-390.(doi:10.1111/j.1469-185X.1950.tb01590.x)
4. Schutz D. TM. 2003 Adaptations to an aquatic life may be responsible for the reversed sexual size dimorphism in the water spider, *Argyroneta aquatica*. *Evol Ecol Res*. **5**,105-117
5. Anderson DS. 1960 The respiratory system of the egg-shell of *Calliphora erythrocephala*. *J Insect Physiol*. **5**,120-128.(doi:10.1016/0022-1910(60)90037-8)
6. Hebets EA, F. Chapman R. 2000 Surviving the flood: plastron respiration in the non-tracheate arthropod *Phrynus marginemaculatus* (Amblypygi: Arachnida). *J Insect Physiol*. **46**,13-19.(doi:10.1016/S0022-1910(99)00096-7)
7. Hinton HE. 1960 Plastron respiration in the eggs of blowflies. *J Insect Physiol*. **4**,176-183.(doi:10.1016/0022-1910(60)90079-2)
8. Thorpe WH, Crisp DJ. 1947 Studies on plastron respiration. *J Exp Biol*. **24**,227-269
9. Hsu SH, Woan K, Sigmund W. 2011 Biologically inspired hairy structures for superhydrophobicity. *Mat Sci Eng R*. **72**,189-201.(doi:Doi 10.1016/J.Mser.2011.05.001)

10. Grémillet D, Tuschy I, Kierspel M. 1998 Body temperature and insulation in diving Great Cormorants and European Shags. *Funct Ecol*. **12**,386-394.(doi:10.1046/j.1365-2435.1998.00199.x)
11. Wilson RP, Hustler K, Ryan PG, Burger AE, Noldeke EC. 1992 Diving Birds in Cold Water: Do Archimedes and Boyle Determine Energetic Costs? *The American Naturalist*. **140**,179-200
12. Rijke AM. 1968 The water repellency and feathure structure of cormorants, *phalogrocorcidae*. *J Exp Biol*. **48**,185-189
13. Gremillet D, Chauvin C, Wilson RP, Le Maho Y, Wanless S. 2005 Unusual feather structure allows partial plumage wettability in diving great cormorants *Phalacrocorax carbo*. *J Avian Biol*. **36**,57-63.(doi:10.1111/j.0908-8857.2005.03331.x)
14. Rijke AM. 1970 Wettability and Phylogenetic Development of Feather Structure in Water Birds. *J Exp Biol*. **52**,469-469
15. Henyemann WW. 1984 Spread-winged behaviour of Double-crested and Flightless Cormorants *Phalacrocorax auritus* and *P. harrisi*: wing drying or thermoregulation? *Ibis*. **126**,230-239
16. Cassie ABD, Baxter S. 1944 Wettability of porous surfaces. *Transactions of Faraday Society*. **40**, 546–551
17. Bormashenko E, Gendelman O, Whyman G. 2012 Superhydrophobicity of Lotus Leaves versus Birds Wings: Different Physical Mechanisms Leading to Similar Phenomena. *Langmuir*. **28**,14992-14997.(doi:10.1021/la303340x)
18. Elowson AM. 1984 Spread-Wing Postures and the Water Repellency of Feathers: A Test of Rijke's Hypothesis. *The Auk*. **101**,371-383
19. Rijke AM. 1987 The Water Repellency of Water-Bird Feathers. *The Auk*. **104**,140-142.(doi:10.2307/4087247)
20. Rijke AM, Jesser WA. 2010 The Feather Structure of Dippers: Water Repellency and Resistance to Water Penetration. *The Wilson Journal of Ornithology*. **122**,563-568.(doi:10.1676/09-172.1)
21. Rijke AM, Jesser WA. 2011 The Water Penetration and Repellency of Feathers Revisited. *The Condor*. **113**,245-254.(doi:10.1525/cond.2011.100113)
22. Rijke AM, Jesser WA, Mahoney SA. 1989 Plumage wettability of the African darter *Anhinga-melanogaster* compared with the double-crested cormorant *Phalacrocorax-auritus*. *Ostrich: Journal of African Ornithology*. **60**,128-128.(doi:10.1080/00306525.1989.9633739)
23. Rijke AM, Jesser WA, Evans SW, Bouwman H. 2000 Water repellency and feather structure of the Blue Swallow *Hirundo atrocaerulea*. *Ostrich*. **71**,143-145.(doi:10.1080/00306525.2000.9639893)
24. Berg JC. 1993.*Wettability*, M. Dekker;
25. Choi W, Tuteja A, Chhatre S, Mabry JM, Cohen RE, McKinley GH. 2009 Fabrics with Tunable Oleophobicity. *Advanced Materials*. **21**,2190-2195.(doi:10.1002/adma.200802502)
26. Stephenson R, Andrews CA. 1997 The effect of water surface tension on feather wettability in aquatic birds. *Can J Zool*. **75**,288-294.(doi:10.1139/z97-036)
27. Young T. 1805 An Essay on the Cohesion of Fluids. *Philosophical Transactions of the Royal Society of London*. **95**,65-87.(doi:10.1098/rstl.1805.0005)
28. Brakke KA. 1992 The Surface Evolver. *Experimental Mathematics*. **1**,141-165.(doi:10.1080/10586458.1992.10504253)

29. Wenzel RN. 1936 Resistance of solid surfaces to water by wetting. *Ind. Eng. Chem.* **28**,988-994.(doi:10.1021/ie50320a024)
30. Cassie ABD, Baxter S. 1944 Wettability of porous surfaces. *Transactions of the Faraday Society*. **40**,546-551.(doi:10.1039/TF9444000546)
31. Bormashenko E, Bormashenko Y, Stein T, Whyman G, Bormashenko E. 2007 Why do pigeon feathers repel water? Hydrophobicity of pennae, Cassie-Baxter wetting hypothesis and Cassie-Wenzel capillarity-induced wetting transition. *J. Colloid Interface Sci.* **311**,212-216.(doi:10.1016/j.jcis.2007.02.049)
32. Tuteja A, Choi W, Mabry JM, McKinley GH, Cohen RE. 2008 Robust omniphobic surfaces. *Proceedings of the National Academy of Sciences*. **105**,18200-18205.(doi:10.1073/pnas.0804872105)
33. Mabry JM, Vij A, Iacono ST, Viers BD. 2008 Fluorinated polyhedral oligomeric silsesquioxanes (F-POSS). *Angewandte Chemie (International Ed. in English)*. **47**,4137-4140.(doi:10.1002/anie.200705355)
34. Chhatre SS, Guardado JO, Moore BM, Haddad TS, Mabry JM, McKinley GH, et al. 2010 Fluoroalkylated Silicon-Containing Surfaces−Estimation of Solid-Surface Energy. *ACS Applied Materials & Interfaces*. **2**,3544-3554.(doi:10.1021/am100729j)
35. Butt H-J, Semprebon C, Papadopoulos P, Vollmer D, Brinkmann M, Ciccotti M. 2013 Design principles for superamphiphobic surfaces. *Soft Matter*. **9**,418-428.(doi:10.1039/C2SM27016A)
36. Marmur A. 2009 Solid-Surface Characterization by Wetting. *Annual Review of Materials Research*. **39**,473-489.(doi:doi:10.1146/annurev.matsci.38.060407.132425)
37. Great Cormorant (*Phalacrocorax carbo*), The Birds of North America Online (A. Poole, Ed.). Ithaca: Cornell Lab of Ornithology

[Internet]. 2000 [cited 07/08/2012]. Available from: http://bna.birds.cornell.edu/bna/species/553/articles/introduction.
38. Marmur A. 2003 Wetting on Hydrophobic Rough Surfaces: To Be Heterogeneous or Not To Be? *Langmuir*. **19**,8343-8348.(doi:10.1021/la0344682)
39. Tuteja A, Choi W, Ma ML, Mabry JM, Mazzella SA, Rutledge GC, et al. 2007 Designing superoleophobic surfaces. *Science*. **318**,1618-1622.(doi:10.1126/science.1148326)
40. Lafuma A, Quere D. 2003 Superhydrophobic states. *Nat Mater*. **2**,457-460